Red blood cell membrane-camouflaged polydopamine and bioactived glass composite nanoformulation for combined chemo/chemodynamic/photothermal therapy

Junhao Zhang [a,b], Yanfang Sun [c,], Luping Ren [a,b], Lianxu Chen [a,b], Lei Nie [d], Amin Shavandi [e], Khaydar E. Yunusov [f], Uladzislau E. Aharodnikau [g], Sergey O. Solomevich [g], Guohua Jiang [a,b,*]*

[a] *School of Materials Science and Engineering, Zhejiang Sci-Tech University, Hangzhou, 310018, China*

[b] *International Scientific and Technological Cooperation Base of Intelligent Biomaterials and Functional Fibers, Hangzhou, 310018, China*

[c] *College of Life Sciences and Medicine, Zhejiang Sci-Tech University, Hangzhou, Zhejiang, 310018, China*

[d] *College of Life Sciences, Xinyang Normal University, Xinyang 464000, China*

[e] *Université libre de Bruxelles (ULB), École polytechnique de Bruxelles, 3BIO10 BioMatter, Avenue F.D. Roosevelt, 50 - CP 165/61, 1050 Brussels, Belgium*

[f] *Institute of Polymer Chemistry and Physics, Uzbekistan Academy of Sciences, Tashkent, 100128, Uzbekistan*

[g] *Research Institute for Physical Chemical Problems of the Belarusian State University, Minsk, 220030, Belarus*

E-mail: katherineyfs@zzstu.edu.cn (Y. Sun)

ghjiang_cn@zstu.edu.cn (G. Jiang)

Abstract: Combinations of different therapeutic strategies, including chemotherapy (CT), chemodynamic therapy (CDT), and photothermal therapy (PTT), are needed to effectively address evolving drug resistance and the adverse effects of traditional cancer treatment. Herein, a camouflage composite nanoformulation (TCBG@PRs), an antitumour agent (tubercidin, Tub) loaded into Cu-doped bioactive glasses (CBGs) and subsequently camouflaged by polydopamine (PDA) and red blood cell membranes (RBCm), was successfully constructed for targeted and synergetic antitumour therapies by combining CT of Tub, CDT of doped copper ions, and PTT of PDA. In addition, the TCBG@PR composite nanoformulation was camouflaged with a red blood cell membrane (RBCm) to improve biocompatibility, longer blood retention times, and excellent cellular uptake properties. It integrated with long circulation and multimodal synergistic treatment (CT, CDT, and PTT) with the benefit of RBCms to avoid immune clearance for efficient targeted delivery to tumor locations, producing an "all in one" nanoplatform. *In vivo* results showed that the TCBG@PR composite nanoformulation prolonged blood circulation and improved tumor accumulation. The combination of CT, CDT, and PTT therapies enhanced antitumour therapeutic activity, and light-triggered drug release reduced systematic toxicity and increases synergistic antitumor effects.

Keywords: Red blood membrane; dopamine; tubercidin; chemodynamic therapy; photothermal therapy; synergistic therapy

1. Introduction

Breast cancer, one of the most prevalent cancers in women worldwide, is a significant public health concern. Despite major advances in diagnosis and therapy [1,2], breast cancer-related mortality remains high. Breast cancer is widely treated with surgery, radiation therapy, endocrine therapy, and chemotherapy. Surgery offers the advantage of tumor removal, providing a definitive diagnosis, and potentially preventing cancer spread; however, surgical risks and possible postoperative repair issues are associated with it [3]. Radiation therapy can destroy remaining cancer cells and be targeted, but it also has the disadvantages of high side effects and limited population applicability [4]. Endocrine therapy effectively tackles hormone receptor-positive cancers, reducing recurrence risk, but is limited to such cancers and long-term risks [5]. Chemotherapy targets cancer cells throughout the body, shrinking tumors and working well in combination; nevertheless, it has side effects, can harm healthy cells, and poses long-term health risks [6,7]. Therefore, the focus of research has shifted to the creation of accurate, effective, and low-side-effect approaches.

As precise and low-side-effect alternatives, photothermal therapy (PTT), chemodynamic therapy (CDT), targeted drug delivery, and immunotherapy have revolutionized breast cancer treatment [8-10]. Recent clinical trials have demonstrated the enhanced efficacy of PTT and CDT in treating tumor cells. CDT effectively converts endogenous H_2O_2 into lethal hydroxyl radicals (·OH) through Fenton or Fenton-like reactions [11-13]. The primary metal catalysts used in CDT, namely iron, copper, and manganese, rely on H_2O_2 in the tumor microenvironment without

requiring external stimuli [14-16]. Additionally, PTT uses the absorption of light energy to generate heat energy, eradicating cancer cells noninvasively [17, 18]. To overcome challenges, such as limitations with photosensitizers and suboptimal H_2O_2 levels in the tumor microenvironment, polydopamine (PDA) has shown promise as a biocompatible and NIR-induced photothermal conversion agent [19, 20]. However, limitations still remain, including insufficient endogenous H_2O_2 in CDT and the dependence of PTT efficacy on the depth and location of tumor tissue [21-22]. Consequently, combining these techniques or their integration with other modalities is gaining interest to optimize therapeutic outcomes and minimize side effects [23-27]. To achieve a synergistic effect, PDA is applied as a photothermal agent to enhance Fenton catalytic activity, while copper or manganese ions serve as CDT agents [28, 29]. Nevertheless, challenges remain, such as inadequate H_2O_2 levels in the tumor microenvironment and inefficient targeting of composite nanoparticles. To overcome some of the limitations of each method, by exploiting the synergistic effect of CT, CDT, and PTT, which can enhance the tumor-killing efficiency and reduce the dosage to minimize the side effects.

Additionally, nanoparticles encapsulated in red blood cell membranes (RBCms) offer a promising therapeutic strategy to reduce side effects by improving targeting, biocompatibility, somatic circulation, and drug accumulation in the tumor [30-34]. Recently, red blood cell membrane-encapsulated PDA nanocomplexes have been widely applied, including mesoporous PDA nanoparticles, intelligent nanocarriers, and multifunctional phototherapy platforms, which enhance drug delivery, enable

combination therapy, mitigate hypoxia, and improve tumor imaging [35-37]. Various drug delivery systems, such as magnetic nanotubes, gold nanotubes, carbon nanotubes, biocompatible nanospheres, dendrimers, liposomes, and micelles, have been investigated for targeted cancer treatment [38]. Notably, bioactive glass (BG) is commonly used in orthopedics and dentistry. It is chosen as a vehicle for drug delivery due to its excellent biocompatibility, bioactivity, and significant tumor growth inhibition properties [39-41]. Chemotherapy drugs, including nabumetone [42], paclitaxel [43], cyclophosphamide [44], docetaxel [45], epirubicin [46], paclitaxel analogues [47], and PARP inhibitors [48], are administered using the bionanosystem for breast cancer treatment. To develop novel therapeutic approaches, tubercidin (Tub), a well-known nucleoside, can undergo different metabolic reactions. It can be phosphorylated by adenosine kinase (AK) and nucleoside diphosphate kinase (NDPK) to form tubercidylate (TBNP) and tubercidyl diphosphate (TBDP), respectively. It can also be deaminated by adenosine deaminase (ADA) to form 7-deaza-inosine (preQ0), which can be further converted to 7-deazaguanine derivatives. Finally, it can be degraded by purine nucleoside phosphorylase (PNP) to form hypoxanthine and ribose-1-phosphate [49-51]. Cellular kinases phosphorylate tubercidin, converting Tub into its triphosphate form, which inhibits protein expression and tumor activity upon integration into DNA or RNA [52,53].

In this study, a biomimetic composite nanoformulation (TCBG@PRs), an antitumor agent (Tub) loaded into Cu-doped bioactive glasses (CBGs) and subsequently camouflaged by PDA and RBCm, has been successfully constructed for

targeted and synergetic antitumor therapies by the combination of CT of Tub, CDT of doped copper ions, and PTT of PDA. In addition, the TCBG@PRs composite nanoformulation was camouflaged with a RBCm to improve biocompatibility, longer blood retention times, and excellent cellular uptake properties. It integrated with long circulation and multimodal synergistic treatment (CT, CDT, and PTT) with the benefit of RBCms to avoid immune clearance for efficient targeted delivery to tumor locations, producing an "all in one" nanoplatform (Figure 1). Moreover, the bioefficacy investigations of these composite nanoformulations (TCBG@PRs) have demonstrated enhanced inhibition in both in vitro cell experiments and in vivo tests on tumor-bearing mice. These findings provide compelling evidence of its potential synergistic therapeutic efficacy.

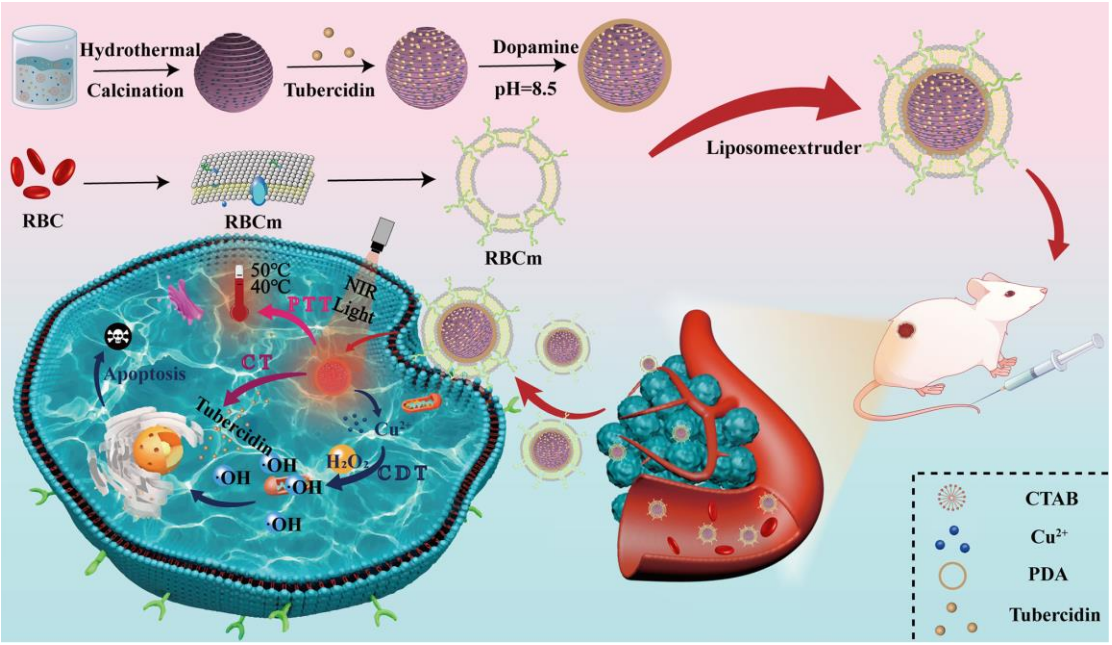

Figure 1. Schematic illustration of the preparation of TCBG@PRs and the synergistic treatment of mice under near-infrared light irradiation.

2. Experimental section

2.1 Materials

Hexadecyltrimethylammonium bromide (CTAB), ethyl acetate (EA), ethyl orthosilicate (TEOS), triethyl phosphate (TEP), calcium nitrate tetrahydrate (CN), copper nitrate trihydrate, dopamine hydrochloride (DA), Tris-HCl buffer (pH = 8.5), fluorescein isothiocyanate (FITC), 2’, 7’-dichlorodihydrofluorescein diacetate (DCFH-DA), and methylene blue solution were purchased from Shanghai Aladdin Biochemical Technology Co., Ltd. Ammonia (AR, 25-28%) was purchased from Hangzhou Gaojing Fine Chemical Co., Ltd. Tubercidin was provided by Shanghai Haoyuan Biomedical Technology Co., Ltd. Sheep blood that had been sterilized and defibrinated was purchased from Nanjing Quanlong Biotechnology Co., Ltd. Hydrogen peroxide was purchased from Shanghai Lingfeng Chemical Reagent Co., Ltd. Kaumas Brilliant Blue staining solution/elution solution, 5,5-dimethyl-1-pyrroline-N-oxide (DMPO), 4',6-diamidino-2-phenylindole (DAPI), a reactive oxygen species (ROS) detection kit, and 3-(4, 5-dimethyl-thiazol-2-yl)-2, 5-diphenyl-tetrazolium bromide (MTT) were acquired from Shanghai Biyuntian Biotechnology Co., Ltd. The red blood cell membrane (RBCms) was obtained according to a protocol with some modifications [54].

2.2 Fabrication of red blood cell membrane-camouflaged composite nanoformulation (TCBG@PRs)

According to previous reports [55,56], the hydrothermal process was used to prepare the CBGs. Then, the CBGs (10 mg) were dispersed in 10 mL of deionized water. The mixed solution consisted of 5 mL of DMSO, and 20 mg of tubercidin was added to the CBGs solution and stirred for 24 h. The Tub-loaded composite

nanoparticles (TCBGs) were separated by centrifugation, and the supernatant was subjected to UV–Vis absorption analysis. The as-prepared TCBGs (20 mg) were redispersed in 10 mL of Tris-HCl buffer (pH = 8.5, 1×10^{-3} mol/L). Then, 10 mg of dopamine hydrochloride was added and stirred for 6 h at room temperature for self-polymerization to form a polydopamine (PDA) layer on the TCBGs (TCBG@Ps). For the camouflation of RBCms onto the surface of TCBG@Ps, an Avanti mini-extruder (LF-1, Ottawa, Canada) was used to repeatedly extrude the mixture of TCBG@Ps and RBCms *via* 400 and 200 nm pores 21 times. Finally, the red blood cell membrane-camouflaged composite nanoformulation (TCBG@PRs) was obtained after removing the excess RBCm by centrifugation.

2.3 Characterization

The hydrodynamic size and zeta potential of CBGs, TCBG@Ps, and TCBG@PRs were characterized by a Zetasizer (Zetasizer Nano ZS, Malvern, UK). UV–vis spectra were obtained from a UV–vis spectrometer (U3900H, Hitachi Corporation, Japan). Transmission electron microscopy (JEM-2100, Japan Electronics Corporation) and scanning electron microscopy (Ultra 55 FE-SEM, Carl Zeiss SMT, Germany) were used to evaluate the morphology and size of the composite nanoparticles. The specific surface area and pore volume were tested by a Brunauer-Emmett-Teller analyser (3H-2000PS1, Bayside Instrument Technology Co. Ltd.). Electron spin resonance (ESR) was used to evaluate the typical peak of ·OH (A300, Bruker, Germany).

2.4 Drug loading and release *in vitro*

The loading (*LE%*) and encapsulation efficiency (*EE%*) of Tub were determined by the following formula:

$$LE\% = \frac{Wm - Wn}{Wm} \times 100\% \tag{1}$$

$$EE\% = \frac{Wm - Wn}{W_{NPs}} \times 100\% \tag{2}$$

where *Wn* is the weight of unloaded Tub in the supernatant, *Wm* is the overall weight of tubercidin, and W_{NPs} is the weight of TCBG@PRs.

In order to assess drug release *in vitro*, 10 mg of TCBG@PRs were sealed into a dialysis bag (MWCO = 500) and then immersed in 60 mL of PBS buffer solution at pH of 7.4, 5.5 and 5.5+NIR. One milliliter of dialysate was collected to test the absorption intensity (λ = 270 nm) at a certain time intervals, and the drug release was determined by a Tub standard curve.

2.5 Photothermal effects *in vitro*

TCBG@PRs solutions (2.5 mL) at different concentrations (0, 25, 50, 100, and 200 μg/mL) were injected into Eppendorf tubes. An infrared thermography device (325, Fotric, America) was used to record their temperature changes under NIR irradiation (808 nm, 1.0 W/cm^2). The temperature changes of the TCBG@PRs solution (200 μg/mL) by four on/off NIR irradiation cycles were used to evaluate their thermal stability.

2.6 Biocompatibility evaluation *in vitro*

Different concentrations of TCBG@PRs in PBS solutions (25, 50, 100, 200, and 400 μg/mL) were coupled with a 5% erythrocyte solution. Then, deionized water and

PBS solutions (0 μg/mL) served as positive and negative controls, respectively. The mixture was then incubated at 37 °C for 6 h. The mixture was centrifuged for 5 min at 3,500 rpm. The absorbance of the mixture at 540 nm was measured using an UV–vis spectrometer. The hemolysis rate was calculated by the formula:

$$Hemolytic\,rate = \frac{A1 - A3}{A2 - A3} \times 100\% \tag{3}$$

where *A1* is the sample absorbance, *A2* is the positive absorbance, and *A3* is the negative absorbance.

2.7 Hydroxyl radical (·OH) generated by TCBG@PRs *in vitro*

TCBG@PRs were dispersed in PBS solution ultrasonically to form different concentrations of 0, 25, 50, 100, and 200 μg/mL. Then, 1 mL of methylene blue (MB) solution (10.0 μg/mL) was added, followed by stirring for 5 min to determine the generation of hydroxyl radicals. The absorption spectra of the mixed solution were recorded using a UV–Vis spectrophotometer. And the MB degradation was tested in 5 min. Additionally, DMPO was used as a spin trap and added to the aqueous solution of TCBG@PRs to detect the generation of ·OH by ESR [57].

2.8 Cell culture and cytotoxicity *in vitro*

Mouse breast cancer 4T1 and L929 cells were provided by the Chinese Academy of Sciences Cell Bank (Shanghai, China). The MTT kit was used to test the cytotoxicity of the as-fabricated composite nanoformulation *in vitro* and evaluate the synergistic inhibitory effect of CBG@Ps, TCBG@Ps, and TCBG@PRs under NIR light excitation. 4T1 cells were inoculated in 96-well plates (100 μL DMEM per well) at 8×10^3 cells per well and then placed at 37 °C in a 5% CO_2 incubator overnight for

culture. Then, the DMEM from the upper layer of the plates was removed, and 100 μL of DMEM containing CBG@Ps, TCBG@Ps, and TCBG@PRs at different concentrations (0, 25, 50, 100, and 200 μg/mL) was added. Each group was additionally equipped with NIR light (808 nm, 1.0 W/cm^2) irradiation. After incubation for 24 h, followed by washing of PBS. The MTT solution (5 mg/mL, 0.5% MTT) was added to the well plate and further incubated for 4 h. Then, the absorbance was measured at 490 nm using a microplate analyser.

Additionally, in another cell culture group, after the DMEM of the orifice plate was removed, the following media were added: (1) and (2) 100 μL of DMEM; (3) and (4) 100 μL of DMEM containing CBG@Ps (200 μg/mL); (5) and (6) 100 μL of DMEM containing TCBG@Ps (200 μg/mL); and (7) and (8) 100 μL of DMEM containing TCBG@PRs (200 μg/mL). After culturing in an incubator for 24 h, groups (2), (4), (6), and (8) were stimulated with NIR light (808 nm, 1.0 W/cm^2) for 10 min, respectively. Then, the upper medium of the pore plate was removed and washed with PBS. Afterwards, 100 μL of DMEM was added and cultured in an incubator for 24 h. The MTT solution (5 mg/mL, 0.5% MTT) was added to the well plate and further incubated for 4 h, and the absorbance was measured at 490 nm using a microplate analyser.

2.9 Intracellular ROS detection

To evaluate intracellular ROS generation, a confocal laser scanning microscope (CLSM, Axio Observer A1, Carl Zeiss) was used with the fluorescent probe DCFH-DA [58]. Briefly, 4T1 cells were seeded in 6-well plates, and the cells were

collected after adding each treatment group for 6 h. After washing with PBS 3 times, DCFH-DA was added, and the cells were incubated at 37 °C for 30 min and washed three times. The level of ROS was detected under CLSM.

2.10 Cellular uptake

The uptake of TCBG@Ps and TCBG@PRs was observed using CLSM. 4T1 cells were incubated at 37 °C for 24 h. The cells were then treated with 100 μL PBS, 100 μL FITC (200 μg/mL), 100 μL TCBG@Ps-FITC (200 μg/mL), or 100 μL TCBG@PRs-FITC (200 μg/mL) in PBS. After incubation for 6 h, the cells were washed with PBS 3 times, and then 1 mL of paraformaldehyde (4%) was added. After incubation for 20 min, the cell nuclei were counterstained with 1 mL of DAPI solution for 15 min and observed by CLSM.

2.11 Tumor model of breast cancer

Five-week-old female BALB/c mice (SPF grade, 18-20 g) were provided by the Zhejiang Center of Laboratory Animals and fed under standard conditions in the Hangzhou Medical College Laboratory Animal Center. All animal experiments were approved by the Institutional Animal Care and Use Committee (acceptance number: ZJCLA-IACUC-20010256) and the Animal Ethics Committee of Zhejiang Sci-Tech University (acceptance number: 2023031402). Tumors were established by subcutaneous injection of 4T1 cells (5×10^5) dispersed in 50 μL of PBS into the right groin of each mouse. After the tumor grew to 50-100 mm^3, the tumor-bearing mice were used in the following experiments.

2.12 Antitumour evaluation *in vivo*

The distribution of free nanocomposite *in vivo* was observed using a small animal imaging system (PerkinElmer, USA). Free Fitc-labelled TCBG@PRs were administered intravenously to 4T1 tumor-bearing mice. At established time points, the mice were dissected, and *in vivo* major organ imaging was recorded using a small animal imaging system. The established tumor-bearing mice were randomly separated into eight groups (3 mice in each group): (1) PBS, (2) PBS + NIR, (3) CBG@Ps, (4) CBG@Ps + NIR, (5) TCBG@Ps, (6) TCBG@Ps + NIR, (7) TCBG@PRs, and (8) TCBG@PRs + NIR, in which the NIR group was stimulated with NIR light (808 nm, 1.0 W/cm^2) for 5 min after tail vein injection for 6 h. The dosage of Tub is 2.5 mg/kg in mice. The real temperature and thermal image of the nanocomposite were recorded using an infrared thermal imager to analyse the temperature change. The tumor-bearing mice in each group were treated on days 0, 2, 4, 6, 8, 10, and 12. The body weight and tumor volume of the mice in each group were measured every 2 days. After euthanasia on day 12, the weight and measured size of the tumor were recorded by dissecting the tumor *in vitro* ($0.5 \times \text{length} \times \text{width}^2$).

2.13 Histological analysis of tumors

The mice were euthanized by injection of pentobarbital sodium solution on day 12. After the tumor was carefully extracted and fixed with 4% formaldehyde, it was embedded in paraffin blocks, sliced, stained with H&E, TUNEL, and Ki67 kits, and mounted on a slide. In addition, the heart, liver, spleen, lung, and kidney of each group of 4T1 tumor-bearing mice were stained with H&E. The pathological conditions of the tumor and main organs in the tumor-bearing mice were observed and

analysed via microscopy.

3. Results and discussion

3.1 Preparation and Characterization of TCBG@PRs

First, a hydrothermal process is used to prepare CBGs. The TEM images of the CBGs show the pineal morphology with voids and the laminar structure (Figure 2a) for drug loading. The homogeneous spherical structure of the CBGs can also be observed in the SEM image (Figure S1a). The CBGs have an average pore volume of 1.11 cm^3/g and a specific surface area of 489.40 m^2/g, as determined by the BET test (Figure S2a). Due to high pore volume and specific surface area, CBGs can be used as carriers to load Tub. After loading with Tub, the average pore volume and specific surface area show a obvious decrease to 0.73 cm^3/g and 387.76 m^2/g (Figure S2b). In addition, the lamellar voids are covered in the TCBGs compared with CBGs (Figure S3), demonstrating the successful loading of the drug. In order to reduce leakage of loaded drug, the PDA layer is further uniformly coated onto TCBG@Ps by means of surface self-polymerization to form a distinguishable rough surface structure [57,58] (Figures 2b and S1b).

An additional membrane structure can be observed around the periphery of TCBG@PRs (Figure 2c). The increase in particle size is caused by the lipid bilayer of the RBCm [61]. However, the mean hydrodynamic diameter of TCBG@PRs increased from 145.6 nm to 160.6 nm after camouflaging by PDA and RBCms (Figure S4), providing a suitable size for endocytosis.

The zeta potentials of the TCBG@Ps and RBCms are -19.8 mV and -9.6 mV,

respectively (Figure 2d), while after camouflaging by the RBCms, they shifted from -19.8 mV to -12.8 mV, which is closer to the value of the RBCms. CBGs can be suitable for chemical dynamic treatment (CDT) because of the doping of copper ions. X-ray photoelectron spectroscopy (XPS) demonstrates the presence of Cu ions in CBGs based on the distribution of Cu elements (Figure 2e), proving the possibility for chemodynamic therapy. The coexistence of Cu^{+} and Cu^{2+} ions is discovered through further examination of the valence states of Cu ions in CBGs (Figure 2f). Energy-dispersive spectroscopy (EDS) reveals the elemental composition of CBGs with amount of ~ 1.91 wt% copper (Figure 2g). Element mapping images show the uniform distribution of Si, O, C, Ca, and Cu in CBGs. The content of the surface membrane proteins of TCBG@PRs was analysed by Kaumas Brilliant Blue staining. Figure 2i shows that the protein bands remained intact, and the types and contents of membrane proteins were basically the same between the RBCm group and the TCBG@PRs group. Meanwhile, the TCBG@Ps group lacks the protein band, indicating that the main protein is preserved during preparation to achieve long-term circulation in the body. Figures S5a shows the hydrodynamic size distribution of TCBG@PRs over a week, no obvious changes in size is observed. In addition, only a slight drug release and zeta potential changes are occured (Figure S5b and c), indicating the excellent stability of the as-prepared TCBG@PRs.

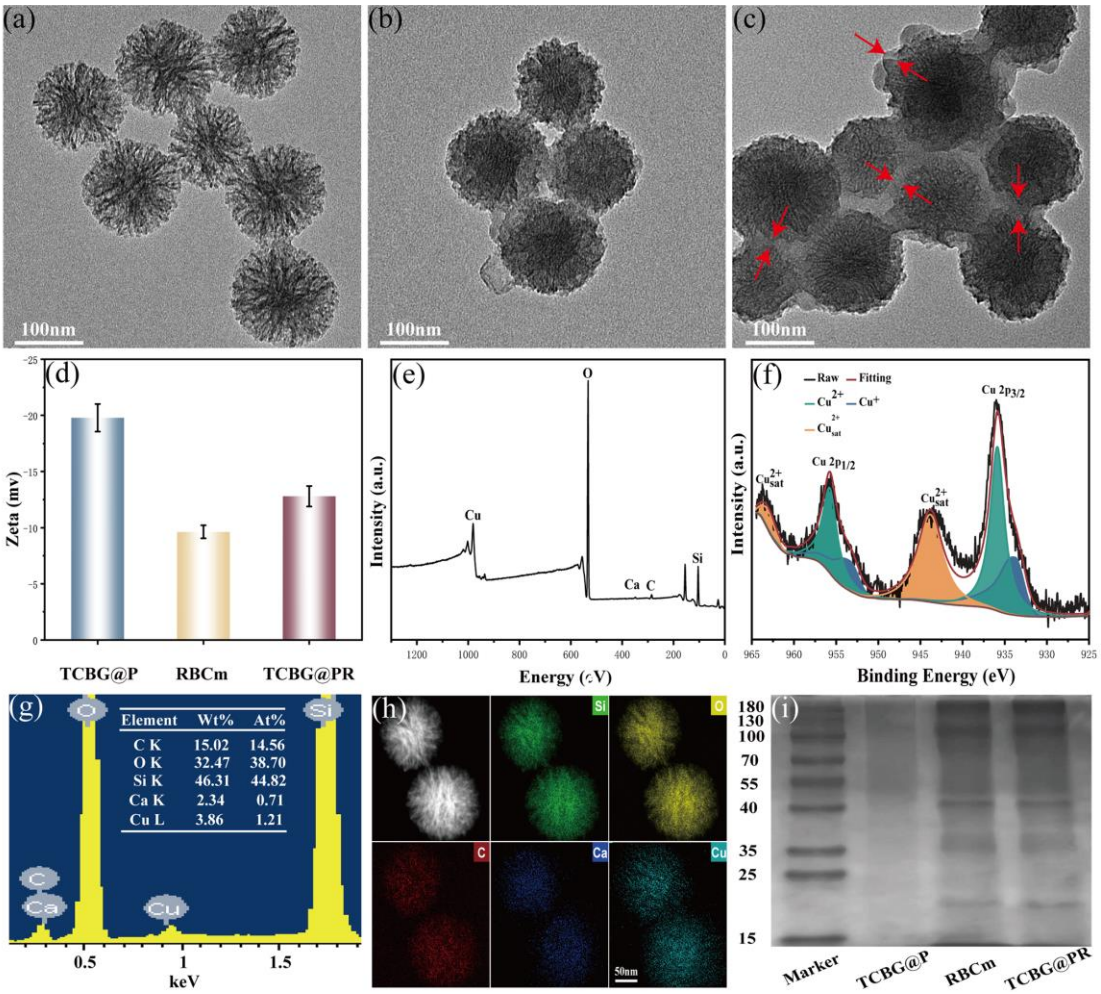

Figure 2. Structural characterization of CBGs, TCBG@Ps, and TCBG@PRs. (a) TEM images of CBGs, (b) TCBG@Ps, and (c) TCBG@PRs with a scale bar of 100 nm; (d) zeta potentials of TCBG@Ps, RBCm, and TCBG@PRs; (e) XPS full spectrum of CBGs and (f) Cu 2p XPS spectrum; (g) EDS spectrum and (h) elemental mapping images of CBGs; (i) SDS-PAGE images of TCBG@Ps, RBCms, and TCBG@PRs.

3.2 Photothermal effect *in vitro*

To assess the photothermal effect of TCBG@PRs, a 1.0 W/cm^2 NIR light model was used as described in a previous study [62]. RBCms decomposes when exposed to NIR light, making the PDA in the outer layer of TCBG@PRs a suitable photothermal agent [63]. Using a thermal imager, the temperature changes of the TCBG@PRs solutions at various concentrations (0, 25, 50, 100, and 200 μg/mL) were recorded. As shown in Figure 3a, the temperatures of TCBG@PRs solutions are increased as the

concentration of TCBG@PRs under NIR irradiation increases. In contrast, almost no temperature change has been observed for the blank solution. The temperature change profiles against NIR irradiation time are shown in Figure 3b. After NIR irradiation for 10 min, the temperature of the solutions reaches 32.4, 38.7, and 43.4 °C with TCBG@PRs concentrations of 25, 50, and 100 μg/mL, respectively. Further increasing the concentration of TCBG@PRs to 200 μg/mL leads to an increase in the temperature of the solution to 52.5 °C under the same NIR light irradiation conditions. As a control, the blank PBS solution only had a slight temperature rise (2.2 °C). To determine the photothermal stability of TCBG@PRs, four NIR irradiation cycles (5 and 5 min for on/off of NIR light) on the TCBG@PRs solution (200 μg/mL) were carried out, as shown in Figure 3c. The temperature peaks of the TCBG@PRs solution are 51.5, 52.6, 53.2, and 52.7 °C, showing a good photothermal stability. Cancer cells are easily killed at above 40 °C [64]. Therefore, the superior photothermal performance of the TCBG@PRs has great potential in treating cancer cells via PTT.

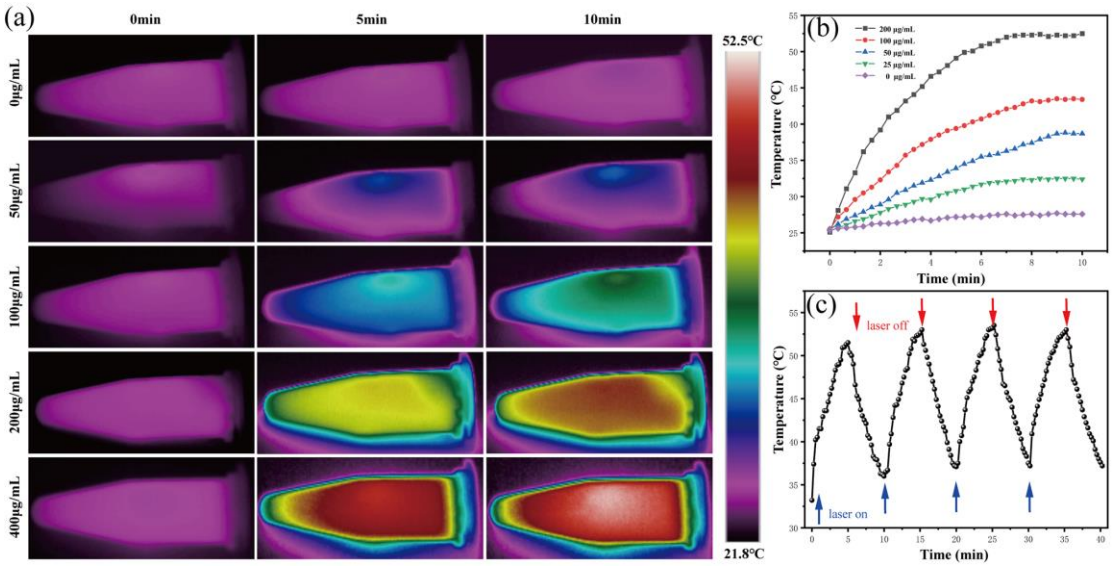

Figure 3. Photothermal performance of TCBG@PRs. (a) Infrared thermal images of TCBG@PRs solutions at different concentrations (0, 25, 50, 100, and 200 μg/mL) under 808 nm near-infrared light irradiation for 0, 5, and 10 min, (b) the temperature change profiles against NIR irradiation for 10 min and (c) time–temperature curve of TCBG@PRs solution (200 μg/mL) under 808 nm near-infrared light irradiation for 4 cycles.

3.3 Drug release and biocompatibility *in vitro*

Due to the high specific surface and pore volume, CBGs can be used as a drug carrier by stirring CBGs aqueous solution and Tub in DMSO solution for 24 h. The loading efficiency (LE %) and encapsulation efficiency (EE %) of Tub are calculated as 18.26% and 81.3%, respectively. CBGs have been shown to possess low chemical durability and to degrade in physiological media, leading to the release of the loaded drug. Figure 4a shows the Tub release profile by incubation of TCBG@PRs in a simulated tumor microenvironment at pH 5.5. In the first 4 h, 29.45% of Tub can be rapidly released from TCBG@PRs. The cumulative Tub release will be improved to 67.81% up to 24 h, and ~76.01% of the released drug will be obtained after a further 24 h incubation. Moreover, after incubation of TCBG@PRs at pH 5.5 under 808 nm light irradiation, more Tub can be released from TCBG@PRs in the first 8 h, with cumulative release to ~79.94%. It may be attributed to the faster thermal decomposition of the shell layer of TCBG@PRs under light irradiation. However, only ~15.12% of the drug can be released in PBS solution with pH 7.4. The increased drug release in an acidic environment can be attributed to the accelerated decomposition of PDA on the surface of TCBG@PRs. This phenomenon proves advantageous for facilitating drug release, specifically within tumor cells. Different concentrations of TCBG@PRs (25~400 μg/mL) were coincubated with erythrocytes

for 6 h, and the hemolysis rates were tested to evaluate their biocompatibility *in vitro*. As shown in Figure 4b, the hemolysis rates of erythrocytes for all samples are less than 5% compared with pure water as a positive control, showing excellent biocompatibility for blood circulation.

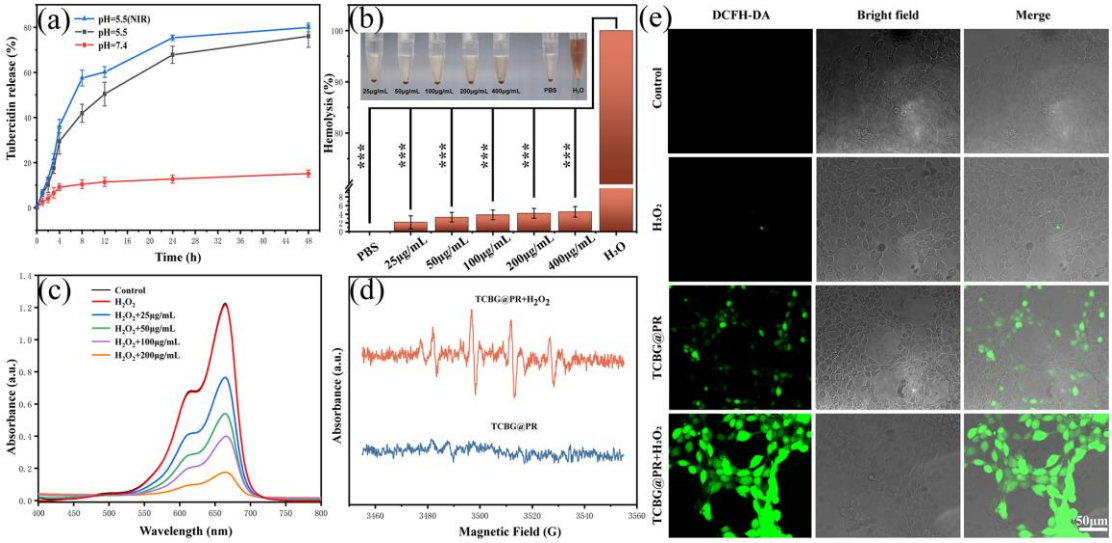

Figure 4. Drug release, biocompatibility, and ROS levels. (a) Tubercidin release profiles of TCBG@PRs in PBS buffer solution at pH 5.5, 7.4, and 5.5+NIR; (b) images and hemolysis rates of different concentrations (0, 25, 50, 100, 200, and 400 μg/mL) of TCBG@PRs solution and H_2O in blood, the data for comparisons are shown to be significant, where *$p < 0.05$, **$p < 0.01$, and *** $p < 0.001$; (c) UV absorption spectra of MB with different concentrations of TCBG@PRs solution (0, 25, 50, 100, and 200 μg/mL); (d) EPR spectra of DMPO trapping ·OH in TCBG@PRs solution with or without H_2O_2; (e) CLSM images of ROS production in 4T1 cells after incubation under different conditions for 5 h.

3.4 Hydroxyl radical (• OH) generated by TCBG@PRs *in vitro*

It is well known that endogenous biological H_2O_2 can be converted into highly deadly hydroxyl (·OH) radicals to destroy tumor cells through metal ion-mediated Fenton or Fenton-like reactions [65]. To determine the production of ·OH, UV absorption was used to qualitatively compare the absorbance of MB (λ_{max} = 665 nm) after incubation with TCBG@PRs. Under the same conditions, the peak shape and position of MB solution have no changed within 5 min, indicating negligible MB

degradation (Figure S6). As shown in Figure 4c, negligible changes also can be observed in the cases of MB solutions with or without H_2O_2 (1 mM). However, the absorbance intensity of MB will be decreased by increasing the concentration of TCBG@PRs increased, demonstrating that more ·OH radicals were produced by the reaction of TCBG@PRs with H_2O_2. It also indicates that TCBG@PRs can generate ·OH radicals to kill cancer cells by consuming of endogenous H_2O_2. In addition, using DMPO as a trapping agent, a quadruple distinctive peak of ·OH (1:2:2:1) can be discovered in the ESR spectrum of the solution containing TCBG@PRs and H_2O_2 (Figure 4d). However, in the case of the solution containing TCBG@PRs, only significant radical signals can be found, indicating the production of ·OH radicals in the presence of TCBG@PRs.

Copper can kill tumor cells by producing ROS through Fenton-like reactions, and the DCFH-DA fluorescent probe was used to assess ROS levels in 4T1 cells following nanoparticle treatment. As shown in Figure 4e, no DCF fluorescence was detected in cells supplemented only with DCFH-DA (control), while a trace of weak green fluorescence signal was observed in cells treated with H_2O_2. However, the green fluorescence signal can be clearly observed in cells treated with TCBG@PRs and TCBG@PRs+H_2O_2. In addition, the green fluorescence in the TCBG@PRs+H_2O_2 group is stronger, suggesting the presence of ROS as the result of Fenton-like reactions by the copper ions. These results suggest that TCBG@PRs have great potential in cancer treatment *in vivo*.

3.6 Cytotoxicity assay and cellular uptake *in vitro*

To investigate the biocompatibility of CBG@Ps, TCBG@Ps, and TCBG@PRs, the MTT assay was evaluated *in vitro*. As shown in Figure 5a, CBG@Ps exhibited higher cell viability even when the concentration increased to 200 μg/mL, indicating the lower cytotoxicity of the drug carriers. In the cases of TCBG@Ps and TCBG@PRs, the cell viabilities are less than 36%, and 4T1 cell termination is increased as TCBG@Ps or TCBG@PRs concentration increased, further confirming the antitumor drug Tub successful loading of antitumour drugs into CBG@Ps. In addition, the cytotoxicity is further enhanced under NIR irradiation due to the photothermal effect of PDA (Figure 5b). Figure 5c shows the cell viability of 4T1 cells coincubated with different materials under the same concentration conditions. Tub-loaded composite nanoparticles with or without NIR irradiation exhibit low cell viability (≦27%), and relatively lower cell viability can be found with NIR irradiation. In addition, composite nanoparticles encapsulated by RBCms and NIR light irradiation (TCBG@PRs+NIR group) had the lowest cell survival rate (3.37%), demonstrating the synergistic effects of targeting RBCms, photothermal effect of PDA, chemodynamic effect of copper ions, and pharmaceutical effect of Tub. CLSM was further used to observe the subcellular drug distribution and release in cells treated with composite nanoparticles.

As shown in Figure 5d, after incubation for 6 h, the TCBG@PRs+FTIC group shows a higher green fluorescence signal in 4T1 cells than the TCBG@Ps+FITC group, further indicating that the RBCms coating onto the surface of composite nanoparticles is beneficial to cellular uptake and enhance the accumulation of

composite nanoformulation at tumor cells. In addition, after 24 h of incubation with L929 cells, the cell viability of TCBG@PRs are above 70%, exhibiting a non-cytotoxic property (Figures S7a and b). These results demonstrate that as-fabricated composite nanoformulation for synergistic therapy shows a good biocompatibility.

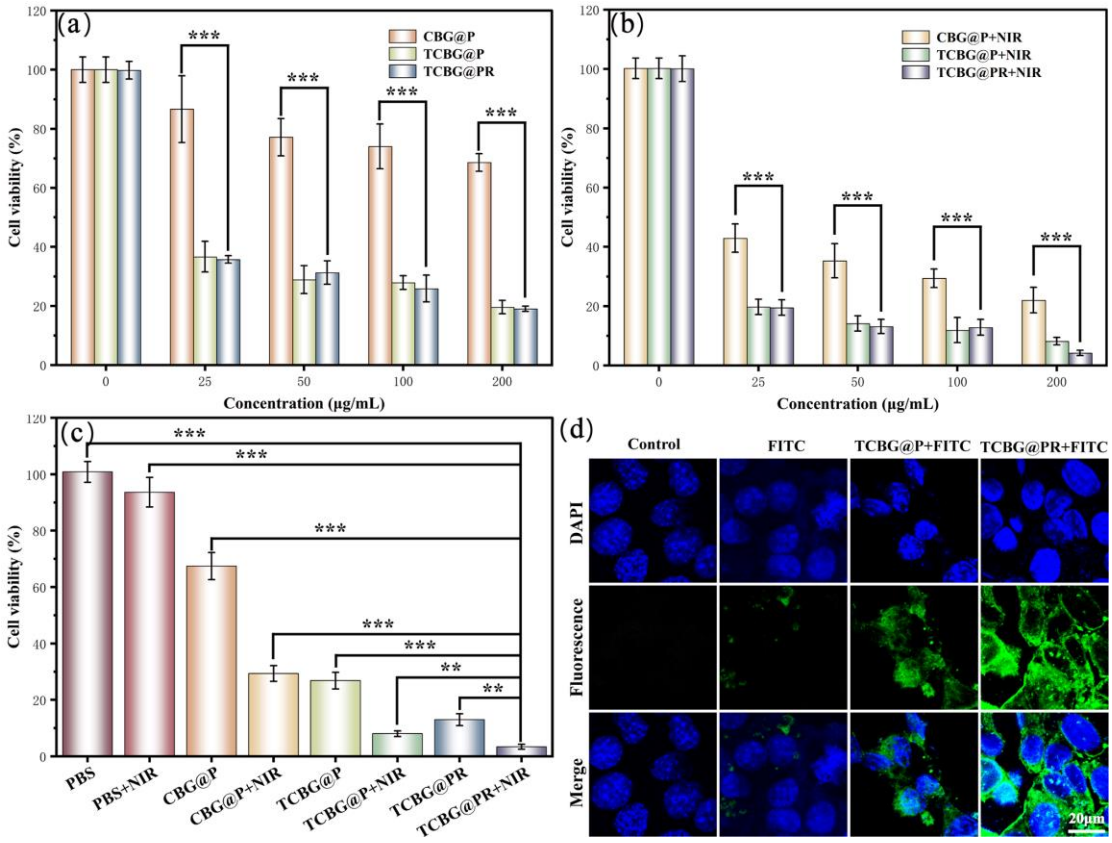

Figure 5. Cytotoxicity assay and cellular uptake. (a) Cell viability of 4T1 cells treated with different concentrations (0, 25, 50, 100, and 200 μg/mL) of CBG@Ps, TCBG@Ps, and TCBG@PRs without or with (b) NIR light irradiation; (c) Cell viability of 4T1 cells coincubated with PBS, CBGs@P, TCBG@Ps, and TCBG@PRs at a concentration of 200 μg/mL with or without NIR light irradiation; (d) Laser confocal images of 4T1 cells coincubated with PBS, FITC, TCBG@Ps-FITC, and TCBG@PRs-FITC for 6 h. The data for comparisons are shown to be significant, where *$p < 0.05$, **$p < 0.01$, and *** $p < 0.001$.

3.7 Antitumour effects *in vivo*

To determine the optical time for NIR light treatment, the dispersion of FITC-labelled TCBG@PRs in the bionic system was analysed *in vivo* in a 4T1

tumor-bearing mouse model at different time intervals. As shown in Figure 6a, bright fluorescence at the tumor site can be observed after tail vein injection for 6 h, indicating the tumor accumulation of TCBG@PRs. Therefore, after drug injection 6 h is selected as the suitable time for NIR irradiation in antitumor operation *in vivo*. However, the liver and kidney shows a weak fluorescence after tail vein injection for 6 h due to the rapid uptake and elimination of Tub [66]. The camouflage of the RBCms allows more drug to accumulate at the tumor site, leading to a relative weaker accumulation in liver and kidney sites. In addition, a strong fluorescence signal can be maintained even after injection for 24 h, indicating that the TCBG@PRs are able to prolong drug residency at the tumor site.

The photothermal performance of the as-fabricated composite nanoparticles *in vivo* was evaluated using infrared thermography. As shown in Figure 6b, the tumor temperatures in the TCBG@Ps, CBG@Ps, and PBS groups were 48.3 °C, 47.6 °C, and 34.4 °C, respectively. The temperature of the TCBG@PRs nanoparticle group quickly rose to 46.6 °C after 5 min of light exposure and reached 53.6 °C after 10 min. Considering that the extremely high temperature (above 50 °C) could generate immunosuppressive cytokines, immune escape of tumor cells, and damage to normal tissues [67], we chose NIR exposure for 5 min in the phototherapeutic experiments.

To investigate antitumor phototherapy *in vivo*, we established a 4T1 tumor-bearing mouse model by subcutaneous injection of 4T1 cells (1×10^6 cells per mouse) into the right flank. When the tumor volume reached ~50 mm^3, the mice were randomly divided and treated with PBS, CBG@Ps, TCBG@Ps, and TCBG@PRs

with or without NIR laser irradiation (808 nm, 1.0 W/cm^2, 10 min) at 6 h after the injection. During the treatment, the mice have almost no weight fluctuation except in the PBS and CBG@Ps groups (Figure 6c). Then, tumor weight and tumor volume were monitored in the following 12 days. Tumor growth was slightly inhibited in the TCBG@Ps and TCBG@PRs groups but obviously inhibited in the TCBG@PRs plus NIR exposure group (Figure 6d and e).

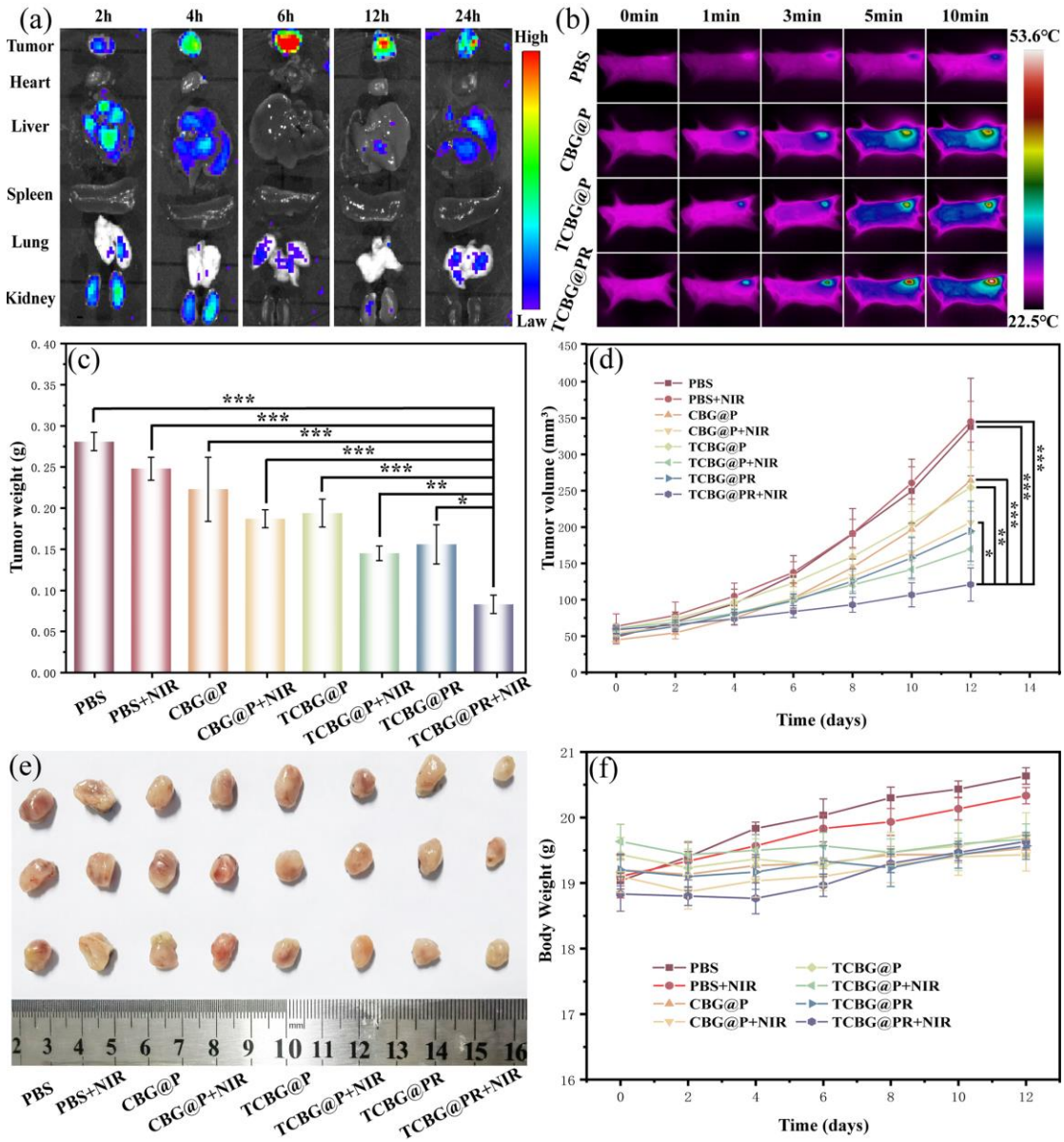

Figure 6. Antitumor effects *in vivo* (a) Ex vivo fluorescence images of major organs and tumor tissue of tumor-bearing mice at different injection times; (b) Thermal image of the tumor-bearing mice at 6 h postinjection of CBG@Ps, TCBG@Ps, and TCBG@PRs under continuous NIR light irradiation for 10 min; (c) Tumor weight of mice under different treatment conditions after 12 days; (d) Time-tumor volume curve under different treatment conditions; (e) Images of tumor tissue morphology of mice treated under different conditions after 12 days; (f) Time-body weight curve of mice under different treatment conditions. The data for comparisons are shown to be significant, where *$p < 0.05$, **$p < 0.01$, and *** $p < 0.001$.

The results indicate that chemotherapy or NIR irradiation alone cannot achieve the efficient antitumor effects. As expected, the synergetic effect of photoinduced and red blood cell membrane-camouflaged nanocomposites was observed in the

TCBG@PRs + NIR group. On the 12th day, the tumor weight of mice in the TCBG@PRs + NIR group was 3.4-fold lighter than that of mice in the PBS group. Digital photo of dissected tumors from all groups directly shows that the TCBG@PRs plus NIR laser irradiation group achieves the highest antitumor efficacy (Figure 6f).

In the H&E staining images of the tumor sections (Figure 7a), for 4T1 tumors receiving PBS as the control, most of the cancer cells retained their normal morphology, whereas the tumor cells were partly destroyed and became necrotic in the single chemotherapy or photothermal treatment groups. Upon laser irradiation, tumors treated with TCBG@Ps plus NIR laser irradiation showed more extensive apoptosis and necrosis than those treated with either TCBG@Ps or CBG@Ps + NIR. In addition, the tumor cells were also partly destroyed in the TCBG@PRs group due to the stronger cellular uptake effect. Most of the tumor cells in the TCBG@PRs + NIR group exhibited the most extensive apoptosis and necrosis in all groups. Additionally, TUNEL immunofluorescence staining also manifested the highest percentage of apoptotic cells in the same group, as verified by the most prevalent and vivid green fluorescence (Figure 7b). Furthermore, Ki67 immunohistochemical staining also confirmed the highest proliferative activity reduction of 4T1 cells subjected to TCBG@PRs+NIR treatment, confirming its capability in preventing tumor metastasis. These results indicate that red blood cell membrane-camouflaged composite nanoparticles (TCBG@PRs) plus NIR irradiation cause severe tumor tissue damage and lead to pronounced tumor inhibition efficacy. In addition, the main organs, including the heart, liver, spleen, lung, and kidney, were collected for

pathological analysis. The H&E staining results of tissues demonstrated that the red blood cell membrane-camouflaged composite nanoparticles (TCBG@PRs) plus NIR irradiation did not lead to obvious pathological abnormalities in the major organs, indicating biosafety for the treatment (Figure S8).

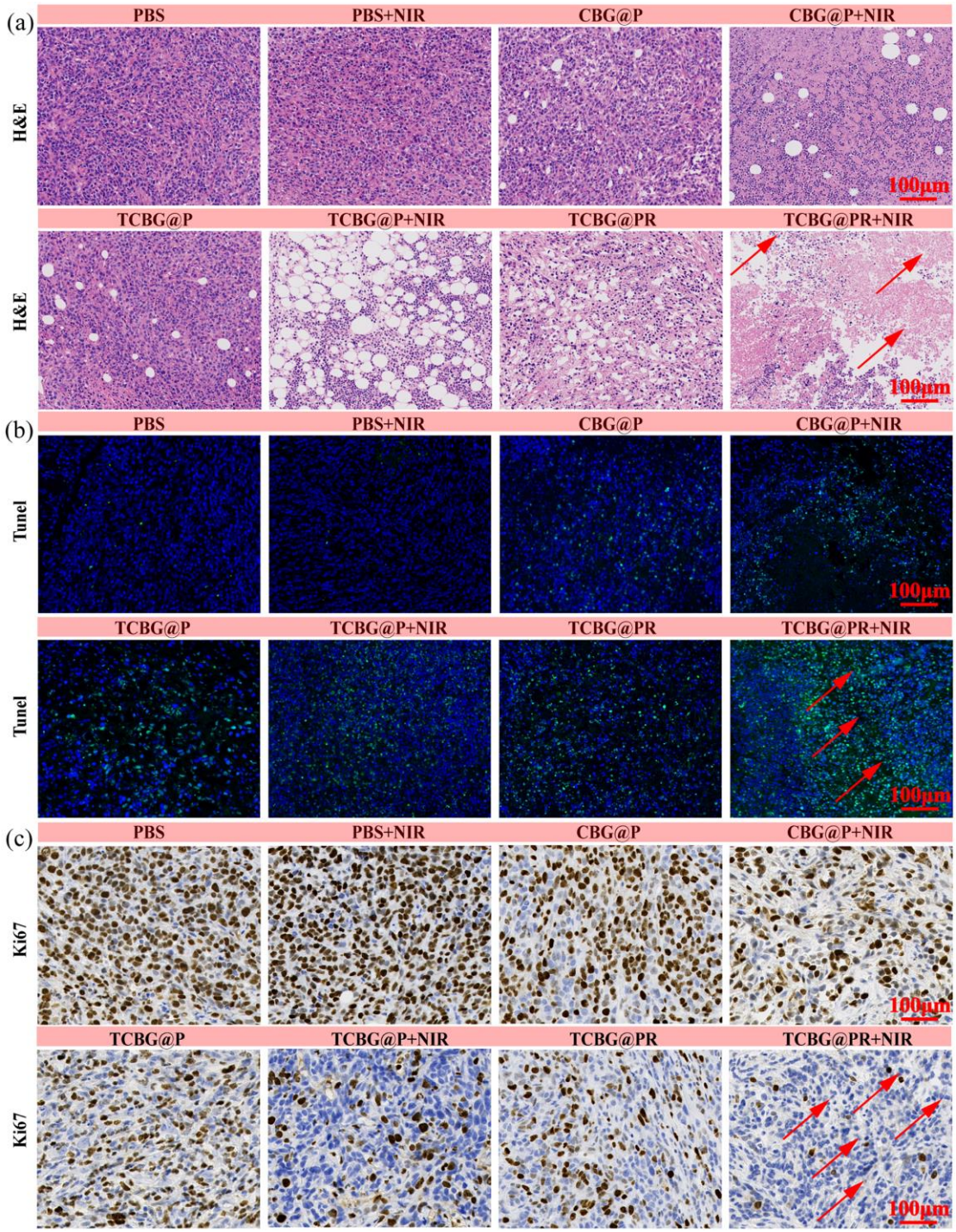

Figure 7. (a) H&E staining, (b) TUNEL staining and (c) Ki67 staining images of tumor tissue

extracted from tumor-bearing mice treated under different conditions for 12 days. The green and brown areas indicate TUNEL-positive and Ki67-positive staining, respectively.

4. Conclusions

In summary, a red blood cell membrane-camouflaged composite nanoformulation as an antitumor agent was successfully constructed for targeted and synergetic cancer therapy by a combination of chemo, chemodynamic, and photothermal therapy. The camouflaging of red blood cell membrane onto the surface of the composite nanoformulation was beneficial to elude immune clearance, leading to stronger cellular uptake and long-term retention at the tumor site. The as-fabricated composite nanoformulation showed NIR photothermal-responsive capability both *in vitro* and *in vivo*. The doped copper ions could generate ·OH radicals to kill cancer cells by consuming endogenous H_2O_2. Under NIR irradiation, the as-fabricated composite nanoformulation could obviously inhibit tumor growth and achieve efficient antitumor effects by synergetic effects. We anticipate that this red blood cell membrane-camouflaged composite nanoformulation will provide a promising strategy for cancer theranostic applications.

Supporting Information

The Supporting Information is available free of charge at https://pubs.acs.org/doi/10.1021/acsbiomaterials.XXXXXXX.

Detailed description of fabrication of CBGs and RBCms, and biocompatibility and stability tests of TCBG@PRs, SEM images of CBGs, TCBG@Ps, and TCBG@PRs, nitrogen adsorption/desorption isotherm and pore size distribution plot of CBGs and TCBGs, TEM and SEM images of TCBGs, hydrodynamic size

distribution of CBGs, TCBG@Ps, and TCBG@PRs in water, the changes of hydrodynamic size distributio, drug release, and zeta potentia of the TCBG@PRs over a week, UV absorption spectra of MB degraded in H2O2 within 5 min, cell viability of L929 cells treated with different concentrations (0, 25, 50, 100, and 200 μg/mL) of TCBG@PRs and tubercidin and Cell viability of L929 cells coincubated with PBS, Tub, CBGs, TCBGs, TCBG@Ps, and TCBG@PRs at a concentration of 200 μg/mL, H&E staining images of major organs extracted from tumor-bearing mice treated under different conditions.

Author Information

Corresponding Author

Guohua Jiang - School of Materials Science and Engineering, Zhejiang Sci-Tech University, Hangzhou, 310018, China; International Scientific and Technological Cooperation Base of Intelligent Biomaterials and Functional Fibers, Hangzhou, 310018, China; Email: ghjiang_cn@zstu.edu.cn

Authors

Junhao Zhang - School of Materials Science and Engineering, Zhejiang Sci-Tech University, Hangzhou, 310018, China; International Scientific and Technological Cooperation Base of Intelligent Biomaterials and Functional Fibers, Hangzhou, 310018, China

Yanfang Sun - College of Life Sciences and Medicine, Zhejiang Sci-Tech University, Hangzhou, Zhejiang, 310018, China

Luping Ren - School of Materials Science and Engineering, Zhejiang Sci-Tech University, Hangzhou, 310018, China; International Scientific and Technological

Cooperation Base of Intelligent Biomaterials and Functional Fibers, Hangzhou, 310018, China

Lianxu Chen - School of Materials Science and Engineering, Zhejiang Sci-Tech University, Hangzhou, 310018, China; International Scientific and Technological Cooperation Base of Intelligent Biomaterials and Functional Fibers, Hangzhou, 310018, China

Lei Nie - College of Life Sciences, Xinyang Normal University, Xinyang 464000, China

Amin Shavandie - Université libre de Bruxelles (ULB), École polytechnique de Bruxelles, 3BIO10 BioMatter, Avenue F.D. Roosevelt, 50 - CP 165/61, 1050 Brussels, Belgium

Khaydar E. Yunusov - Institute of Polymer Chemistry and Physics, Uzbekistan Academy of Sciences, Tashkent, 100128, Uzbekistan

Uladzislau E. Aharodnikau - Research Institute for Physical Chemical Problems of the Belarusian State University, Minsk, 220030, Belarus

Sergey O. Solomevich - Research Institute for Physical Chemical Problems of the Belarusian State University, Minsk, 220030, Belarus

Author contributions

J. Z., L. R., and L. C. produced composite nanoformulations and performed cell and animal experiments; J. Z., Y. S. and G. J. analysed the results and wrote the draft of manuscript; Y. S. and G. J. conceived the idea and designed the experiments; L. N. and A. S. provided suggestions and commented on the manuscript; K. E. Y., U. E. A.,

and S. O. S. reviewed the manuscript.

Declaration of Competing Interest

The authors declare that they have no known competing financial interests or personal relationships that could have appeared to influence the work reported in this paper.

Acknowledgements

This work was financially supported by the Huadong Medicine Joint Funds of the Zhejiang Provincial Natural Science Foundation of China under Grant No. LHDMZ23H300003 and the National Natural Science Foundation of China under Grant No. 51873194.

References

(1) Siegel, R. L.; Miller, K. D.; Wagle, N. S.; Jemal, A., Cancer Statistics, 2023. *CA Cancer J. Clin.* **2023**, *73 (1)*, 17-48, DOI: 10.3322/caac.21763.

(2) Arnold, M.; Morgan, E.; Rumgay, H.; Mafra, A.; Singh, D.; Laversanne, M.; Vignat, J.; Gralow, J. R.; Cardoso, F.; Siesling, S.; Soerjomataram, I., Current and Future Burden of Breast Cancer: Global Statistics for 2020 and 2040. *Breast* **2022**, *66*, 15-23, DOI: 10.1016/j.breast.2022.08.010.

(3) Gui, Y.; Liu, X.; Chen, X.; Yang, X.; Li, S.; Pan, Q.; Luo, X.; Chen, L., A Network Meta-Analysis of Surgical Treatment in Patients with Early Breast Cancer. *J. Natl. Cancer Inst.* **2019**, *111 (9)*, 903-915, DOI: 10.1093/jnci/djz105.

(4) Bradley, J. A.; Mendenhall, N. P., Novel Radiotherapy Techniques for Breas t Cancer. *Annu. Rev. Med.* **2018**, *69*, 277-288, DOI: 10.1146/annurev-med-0 42716-103422.

(5) Jackisch, C., Overcoming Endocrine Resistance in Neoadjuvant Endocrine Therapy for Early Breast Cancer. *Lancet Oncol.* **2019**, *20 (9)*, 1185-1187, DOI: 10.1016/S1470-2045(19)30500-5.

(6) Medina, S. H.; Bush, B.; Cam, M.; Sevcik, E.; DelRio, F. W.; Nandy, K.; Schneider, J. P., Identification of A Mechanogenetic Link Between Substrate Stiffness and Chemotherapeutic Response in Breast Cancer. *Biomaterials* **2019**, *202*, 1-11, DOI: 10.1016/j.biomaterials.2019.02.018.

(7) Waks, A. G.; Winer, E. P., Breast Cancer Treatment: A Review. *JAMA* **2019**, *321 (3)*, 288-300, DOI: 10.1001/jama.2018.19323.

(8) Bou-Dargham, M. J.; Draughon, S.; Cantrell, V.; Khamis, Z. I.; Sang, Q. A., Advancements in Human Breast Cancer Targeted Therapy and Immunotherapy. *J. Cancer* **2021**, *12 (23)*, 6949-6963, DOI: 10.7150/jca.64205.

(9) Liu, T.; Song, S.; Wang, X.; Hao, J., Small-molecule Inhibitors of Breast Cancer-Related Targets: Potential Therapeutic Agents for Breast Cancer. *Eur. J. Med. Chem.* **2021**, *210*, 112954, DOI: 10.1016/j.ejmech.2020.112954.

(10) Lau, K. H.; Tan, A. M.; Shi, Y., New and Emerging Targeted Therapies fo r Advanced Breast Cancer. *Int. J. Mol. Sci.* **2022**, *23 (4)*, 2288, DOI: 10.33 90/ijms23042288.

(11) Hu, Z.; Xu, C.; Liang, Y.; Liu, T.; Tian, H.; Zhang, Y., Multifunctional Drug Delivery Nanoparticles Based on MIL-100 (Fe) for Photoacoustic Imaging-Guided Synergistic Chemodynamic/Chemo/Photothermal Breast Cancer Therapy. *Mater. Design* **2022**, *223*, 111132, DOI: 10.1016/j.matdes.2022.111132.

(12) Gao, L.; Xuan, X.; Sui, M.; Wang, J.; Wang, Y.; Zhang, H., Nanoreactor Activated in Situ for Starvation-Chemodynamic Therapy of Breast Cancer. *J. Drug Target* **2022**, *30 (7)*, 767-776, DOI: 10.1080/1061186X.2022.2062598.

(13) Pan, Y.; Xu, C.; Deng, H.; You, Q.; Zhao, C.; Li, Y.; Gao, Q.; Akakuru, O. U.; Li, J.; Zhang, J.; Wu, A.; Chen, X., Localized NIR-II Laser Mediated Chemodynamic Therapy of Glioblastoma. *Nano Today* **2022**, *43*, 101435, DOI: 10.1016/j.nantod.2022.101435.

(14) Chen, M.; Yang, J.; Zhou, L.; Hu, X.; Wang, C.; Chai, K.; Li, R.; Feng, L.; Sun, Y.; Dong, C.; Shi, S., Dual-Responsive and ROS-Augmented Nanoplatform for

Chemo/Photodynamic/Chemodynamic Combination Therapy of Triple Negative Breast Cancer. *ACS Appl. Mater. Interfaces* **2022**, *14 (1)*, 57-68, DOI: 10.1021/acsami.1c14135.

(15) Zhang, J.; Li, P.; Wang, T.; Li, J.; Yun, K.; Zhang, X.; Yang, X., A Copper Nanocluster-based Multifunctional Nanoplatform for Augmented Chemo/Chemodynamic/Photodynamic Combination Therapy of Breast Cancer. *Pharmacol. Res.* **2023**, *187*, 106632, DOI: 10.1016/j.phrs.2022.106632.

(16) Ming, L.; Song, L.; Xu, J.; Wang, R.; Shi, J.; Chen, M.; Zhang, Y., Smart Manganese Dioxide-Based Lanthanide Nanoprobes for Triple-Negative Breast Cancer Precise Gene Synergistic Chemodynamic Therapy. *ACS Appl. Mater. Interfaces* **2021**, *13 (30)*, 35444-35455, DOI: 10.1021/acsami.1c08927.

(17) Alamdari, S. G.; Amini, M.; Jalilzadeh, N.; Baradaran, B.; Mohammadzadeh, R.; Mokhtarzadeh, A.; Oroojalian, F., Recent Advances in Nanoparticle-Based Photothermal Therapy for Breast Cancer. *J. Control. Release* **2022**, *349*, 269-303, DOI: 10.1016/j.jconrel.2022.06.050.

(18) Kadkhoda, J.; Tarighatnia, A.; Tohidkia, M. R.; Nader, N. D.; Aghanejad, A., Photothermal Therapy-Mediated Autophagy in Breast Cancer Treatment: Progress and Trends. *Life Sci.* **2022**, *298*, 120499, DOI: 10.1016/j.lfs.2022.120499.

(19) Yu, H.; Yan, J.; Li, Z.; Song, T.; Ning, F.; Tan, J.; Sun, Y., Enhanced Photothermal-Ferroptosis Effects Based on RBCm-Coated PDA Nanoparticles for Effective Cancer Therapy. *J. Mater. Chem. B* **2023**, *11 (2)*, 415-429, DOI: 10.1039/d2tb02329f.

(20) Wu, C.-G.; Liang, J.-L.; Wang, X.; Zhou, X.; Cai, X.; Xu, J.; Wang, M.; Wang, W.-B.; Ma, D.; Xue, W., Light-activated Nitric-Oxide Overproduction Theranostic Nanoplatform Based on Long-Circulating Biomimetic Nanoerythrocyte for Enhanced Cancer Gas Therapy. *Sci. Chi. Chem.* **2021**, *64 (10*), 1796-1810, DOI: 10.1007/s11426-021-1045-9.

(21) Li, J. X.; Zhang, L. M.; Liu, C. C.; Wu, Q. N.; Li, S. P.; Lei, X. P.; Huang, Y. G.; Feng, G. N.; Yu, X. Y.; Sun, X. Q.; Guo, Z. M.; Fu, J. J., Doxorubicin-Loaded Hydrogen Peroxide Self-Providing Copper Nanodots for Combination of Chemotherapy and Acid-Induced Chemodynamic Therapy Against Breast Cancer. *J. Colloid Interface Sci.* **2021**, *593*, 323-334, DOI: 10.1016/j.jcis.2021.02.085.

(22) Malviya, R.; Singh, A. K.; Moharana, A.; Prajapati, V. K.; Nirmal, A. K., Photodynamic Therapy of Cancer: Quality and Prospective of Therapy based on Photosensitizer. *Curr. Cancer Ther. Rev.* **2023**, *19 (3)*, 223-236, DOI: 10.2174/1573394719666230119142053.

(23) Zhang, X. Y.; Jiang, G. H.; Song, G.; Liu, T. Q.; Sun, Y. F.; Zeng, Z. Y., Fabrication of h-MnO2@PDA Composite Nanocarriers for Enhancement of Anticancer Cell Performance by Photo-Chemical Synergetic Therapies. *Front Mater. Sci.* **2021**, *15 (2)*, 291-298, DOI: 10.1007/s11706-021-0553-9.

(24) Song, G.; Jiang, G. H.; Liu, T. Q.; Zhang, X. Y.; Zeng, Z. Y.; Wang, R. F.; Li, P. F.; Yang, Y. H., Separable Microneedles for Synergistic Chemo-Photothermal Therapy against Superficial Skin Tumors. *ACS Biomater. Sci. Eng.* **2020**, *6 (7)*, 4116-4125, DOI: 10.1021/acsbiomaterials.0c00793.

(25) Yin, W.; Tian, L.; Wang, S.; Zhang, D.; Guo, S.; Lang, M., Co-Delivery Systems of Paclitaxel Prodrug for Targeted Synergistic Therapy of Breast Cancer. *J. Drug Deliv. Sci. Tec.* **2022**, *69*, 103157, DOI: 10.1016/j.jddst.2022.103157.

(26) Song, G.; Sun, Y. F.; Liu, T. Q.; Zhang, X. Y.; Zeng, Z. Y.; Wang, R.F.; Li, P. F.; Li, C. H.; Jiang, G. H., Transdermal Delivery of Cu-Doped Polydopamine Using Microneedles for Photothermal and Chemodynamic Synergistic Therapy Against Skin Melanoma. *Chem. Eng. J.* **2021**, *426*, 130790, DOI: 10.1016/j.cej.2021.130790.

(27) Ruan, L. M.; Song, G.; Zhang, X. Y.; Liu, T. Q.; Sun, Y. F.; Zhu, J. L.; Zeng, Z. Y.; Jiang, G. H., Transdermal Delivery of Multifunctional CaO_2@ Mn-PDA Nanoformulations by Microneedles for NIR-Induced Synergistic Th erapy Against Skin Melanoma. *Biomater. Sci.* **2021**, *9 (20)*, 6830-6841, DO I: 10.1039/d1bm01117k.

(28) Xiao, Z.; Zuo, W.; Chen, L.; Wu, L.; Liu, N.; Liu, J.; Jin, Q.; Zhao, Y.; Zhu, X., H_2O_2 Self-Supplying and GSH-Depleting Nanoplatform for Chemodynamic Therapy Synergetic Photothermal/Chemotherapy. *ACS Appl. Mater. Interfaces* **2021**, *13 (37)*, 43925-43936, DOI: 10.1021/acsami.1c10341.

(29) Wang, M.; Zhou, G.; Pan, Y.; Xue, Y.; Zhu, S.; Yan, Y.; Yuan, H.; Li, S.; Huang, Q., Design and Fabrication of Cascade Novel Fenton Catalytic Nanocomposite as Theranostic Agent for Chemodynamic/Photothermal Synergistic Tumor Therapy. *Mater. Design* **2022**, *219*, 110794, DOI: 10.1016/j.matdes.2022.110794.

(30) Marshall, S. K.; Angsantikul, P.; Pang, Z.; Nasongkla, N.; Hussen, R. S.

D.; Thamphiwatana, S. D., Biomimetic Targeted Theranostic Nanoparticles f or Breast Cancer Treatment. *Molecules* **2022**, *27 (19)*, 6473, DOI: 10.3390/ molecules27196473.

(31) Ren, L.; Qiu, L.; Huang, B.; Yin, J.; Li, Y.; Yang, X.; Chen, G., Preparati on and Characterization of Anti-Cancer Crystal Drugs Based on Erythrocyte Membrane Nanoplatform. *Nanomaterials* **2021**, *11 (10)*, 2513, DOI: 10.339 0/nano11102513.

(32) Zhou, J.; Kroll, A. V.; Holay, M.; Fang, R. H.; Zhang, L., Biomimetic Nanotechnology toward Personalized Vaccines. *Adv. Mater.* **2020**, *32 (13)*, e1901255, DOI: 10.1002/adma.201901255.

(33) Wang, H.; Wu, J.; Williams, G. R.; Fan, Q.; Niu, S.; Wu, J.; Xie, X.; Zhu, L. M., Platelet-Membrane-Biomimetic Nanoparticles for Targeted Antitumor Drug Delivery. *J. Nanobiotechnology* **2019**, *17 (1)*, 60, DOI: 10.1186/s12951-019-0494-y.

(34) Wang, H.; Bremner, D. H.; Wu, K.; Gong, X.; Fan, Q.; Xie, X.; Zhang, H.; Wu, J.; Zhu, L.-M., Platelet Membrane Biomimetic Bufalin-Loaded Holl ow MnO2 Nanoparticles for MRI-Guided Chemo-Chemodynamic Combined Therapy of Cancer. *Chem. Eng. J.* **2020**, *382*, 122848, DOI: 10.1016/j.cej.20 19.122848.

(35) Zhang, L.; Huang, P.; Huang, S.; Wang, T.; Chen, S.; Chen, Z.; Zhou, Y.; Qin, L., Development of Ligand Modified Erythrocyte Coated Polydopamine Nanomedicine to Codeliver Chemotherapeutic Agent and Oxygen for

Chemo-Photothermal Synergistic Cancer Therapy. *Int. J. Pharm.* **2022**, *626*, 122156, DOI: 10.1016/j.ijpharm.2022.122156.

(36) Wang, H.; Williams, G. R.; Xie, X.; Wu, M.; Wu, J.; Zhu, L. M., Stealth Polydopamine-Based Nanoparticles with Red Blood Cell Membrane for the Chemo-Photothermal Therapy of Cancer. *ACS Appl. Bio. Mater.* **2020**, *3 (4)*, 2350-2359, DOI: 10.1021/acsabm.0c00094.

(37) Zhang, Y.; Yue, X.; Yang, S.; Li, X.; Cui, L.; Cui, X.; Shi, Y.; Liu, Z.; Guo, X.; Li, Y., Long Circulation and Tumor-Targeting Biomimetic Nanoparticles for Efficient Chemo/Photothermal Synergistic Therapy. *J. Mater. Chem. B* **2022**, *10 (26)*, 5035-5044, DOI: 10.1039/d2tb00748g.

(38) Ashfaq, U. A.; Riaz, M.; Yasmeen, E.; Yousaf, M. Z., Recent Advances in Nanoparticle-Based Targeted Drug-Delivery Systems Against Cancer and Role of Tumor Microenvironment. *Crit. Rev. Ther. Drug Carrier Syst.* **2017**, *34 (4)*, 317-353, DOI: 10.1615/CritRevTherDrugCarrierSyst.2017017845.

(39) Shearer, A.; Montazerian, M.; Mauro, J. C., Modern Definition of Bioactive Glasses and Glass-Ceramics. *J. Non-Cryst. Solids* **2023**, *608*, 122228, DOI: 10.1016/j.jnoncrysol.2023.122228.

(40) Nawaz, Q.; Fuentes-Chandía, M.; Tharmalingam, V.; Ur Rehman, M. A.; Leal-Egaña, A.; Boccaccini, A. R., Silibinin Releasing Mesoporous Bioactive Glass Nanoparticles with Potential for Breast Cancer Therapy. *Ceram. Int.* **2020**, *46 (18)*, 29111-29119, DOI: 10.1016/j.ceramint.2020.08.083.

(41) Sui, B.; Zhao, J.; Ding, T.; Ruan, M.; Sun, J.; Liu, X., Cell Membrane

Camouflaged Mesoporous Bioactive Glass Nanoparticles Embedding Glucose Oxidase for Enhancing Targeted Anti-Tumor Catalytic Therapy. *AppL. Mater. Today* **2023**, *32*, 101813, DOI: 10.1016/j.apmt.2023.101813.

(42) Ozaki, Y.; Tsurutani, J.; Mukohara, T.; Iwasa, T.; Takahashi, M.; Tanabe, Y.; Kawabata, H.; Masuda, N.; Futamura, M.; Minami, H.; Matsumoto, K.; Yoshimura, K.; Kitano, S.; Takano, T., Data of Programmed Death-Ligand 1 Expression and VEGF: Nivolumab, Bevacizumab and Paclitaxel For HER2-Negative Metastatic Breast Cancer. *Data Brief* **2022**, *45*, 108558, DOI: 10.1016/j.dib.2022.108558.

(43) Yuan, H.; Guo, H.; Luan, X.; He, M.; Li, F.; Burnett, J.; Truchan, N.; Sun, D., Albumin Nanoparticle of Paclitaxel (Abraxane) Decreases while Taxol Increases Breast Cancer Stem Cells in Treatment of Triple Negative Breast Cancer. *Mol. Pharm.* **2020**, *17 (7)*, 2275-2286, DOI: 10.1021/acs.molpharmaceut.9b01221.

(44) Hu, W.; Song, M.; Li, L., Grading Evaluation of Cardiotoxicity in Patients with Breast Cancer Treated with Adjuvant Paclitaxel Anthracycline/Cyclophosphamide Chemotherapy: A Meta-Analysis. *Comput. Math. Methods Med.* **2022**, *2022*, 7963146, DOI: 10.1155/2022/7963146.

(45) Stoicescu, E. A.; Burcea, M.; Iancu, R. C.; Zivari, M.; Popa Cherecheanu, A.; Bujor, I. A.; Rastoaca, C.; Iancu, G., Docetaxel for Breast Cancer Treatment-Side Effects on Ocular Surface, a Systematic Review. *Processes* **2021**, *9 (7)*, 1086, DOI: 10.3390/pr9071086.

(46) Hu, W.; Lv, K.; Teng, R.; Chen, J.; Xu, C.; Jin, L.; Chen, Y.; Zhao, W., Pegylated

Liposomal Doxorubicin Versus Epirubicin as Adjuvant Therapy for Stage I-III Breast Cancer. *Front. Genet.* **2021**, *12*, 746114, DOI: 10.3389/fgene.2021.746114.

(47) Xie, C.; Cui, Y.; Li, L.; Zhang, M.; Liu, H.; Lin, H., Synthesis and Biological Activity of C-7, C-9 and C-10 Modified Taxane Analogues from 1-Deoxybaccatin VI. *Bioorg. Med. Chem.* **2020**, *28 (21)*, 115736, DOI: 10.1016/j.bmc.2020.115736.

(48) Cortesi, L.; Rugo, H. S.; Jackisch, C., An Overview of PARP Inhibitors for the Treatment of Breast Cancer. *Target Oncol.* **2021**, *16 (3)*, 255-282, DOI: 10.1007/s11523-021-00796-4.

(49) Zheng, B.; Guo, M.; Song, X.; Miao, Y.; Pang, M.; Ming, D., Reversing the Systemic Biotoxicity of Nanomaterials by Downregulating ROS-related Signaling Pathways in the Multi-Organs of Zebrafish Embryos. *Mater. Chem. Front.* **2021**, *5 (11)*, 4231-4243, DOI: 10.1039/d1qm00193k.

(50) Wieder, C.; Frainay, C.; Poupin, N.; Rodriguez-Mier, P.; Vinson, F.; Cooke, J.; Lai, R. P.; Bundy, J. G.; Jourdan, F.; Ebbels, T., Pathway Analysis in Metabolomics: Recommendations for the use of Over-Representation Analysis. *PLoS Comput. Biol.* **2021**, *17 (9)*, e1009105, DOI: 10.1371/journal.pcbi.1009105.

(51) D'Errico, S.; Falanga, A. P.; Capasso, D.; Di Gaetano, S.; Marzano, M.; Te rracciano, M.; Roviello, G. N.; Piccialli, G.; Oliviero, G.; Borbone, N., Pro bing the DNA Reactivity and the Anticancer Properties of a Novel Tuberci din-Pt(II) Complex. *Pharmaceutics* **2020**, *12 (7)*, 627, DOI: 10.3390/pharma ceutics12070627.

(52) Pastor-Anglada, M.; Perez-Torras, S., Emerging Roles of Nucleoside Transporters.

Front. Pharmacol. **2018**, *9*, 606, DOI: 10.3389/fphar.2018.00606.

(53) A. Mulamoottil, V., Tubercidin and Related Analogues: An Inspiration for 50 Years in Drug Discovery. *Curr. Org. Chem.* **2016**, *20 (8)*, 830-838, DOI: 10.2174/1385272819666150803231652.

(54) Chai, Z.; Hu, X.; Wei, X.; Zhan, C.; Lu, L.; Jiang, K.; Su, B.; Ruan, H.; Ran, D.; Fang, R. H.; Zhang, L.; Lu, W., A Facile Approach to Functionalizing Cell Membrane-coated Nanoparticles with Neurotoxin-derived Peptide for Brain-targeted Drug Delivery. *J. Control. Release* **2017**, *264*, 102-111, DOI: 10.1016/j.jconrel.2017.08.027.

(55) Li, X.; Liang, Q.; Zhang, W.; Li, Y.; Ye, J.; Zhao, F.; Chen, X.; Wang, S., Bio-Inspired Bioactive Glasses for Efficient MicroRNA and Drug Delivery. *J. Mater. Chem. B* **2017**, *5 (31)*, 6376-6384, DOI: 10.1039/c7tb01021d.

(56) Xu, B.; Cao, Q. Y.; Zhang, Y.; Yu, W. J.; Zhu, J. Y.; Liu, D. P.; Jiang, G. H., Microneedles Integrated with ZnO Quantum-Dot-Capped Mesoporous Bioactive Glasses for Glucose-Mediated Insulin Delivery. *ACS Biomater. Sci. Eng.* **2018**, *4 (7)*, 2473-2483, DOI: 10.1021/acsbiomaterials.8b00626.

(57) Rutely, C. B.; Jean, M. F.; Walter, Z. T.; Xochitl, D. B.; Mika, S., Towards Reliable Quantification of Hydroxyl Radicals in the Fenton Reaction using Chemical Probes. *RSC Adv.* **2018**, *8 (10)*, 5321-5330, DOI: 10.1039/c7ra13209c.

(58) Hans, C.; Saini, R.; Sachdeva, M. U. S.; Sharma, P., 2',7'-Dichlorofluorescein (DCF) or 2',7'-Dichlorodihydrofluorescein Diacetate (DCFH2-DA) to Measure Reactive Oxygen Species in Erythrocytes. *Biomed Pharmacother* **2021**, *138*,

111512, DOI: 10.1016/j.biopha.2021.111512.

(59) Qu, F.; Guo, Z.; Jiang, D.; Zhao, X.-E., In Situ Growth of Polydopamine on Surface of Covalent Organic Frameworks under the Catalysis of Acid Phosphatase for Dopamine Detection. *Chinese Chem. Lett.* **2021**, *32 (11)*, 3368-3371, DOI: 10.1016/j.cclet.2021.04.010.

(60) Gong, X.; Wang, T.; Zhang, Z.; Wei, X., A Novel and Non-Toxic Dopamine Detection Method Based on Self-Polymerisation of Dopamine. *J. Exp. Nanosci.* **2020**, *15 (1)*, 233-241, DOI: 10.1080/17458080.2020.1757657.

(61) Sun, H.; Su, J.; Meng, Q.; Yin, Q.; Chen, L.; Gu, W.; Zhang, P.; Zhang, Z.; Yu, H.; Wang, S.; Li, Y., Cancer-Cell-Biomimetic Nanoparticles for Targeted Therapy of Homotypic Tumors. *Adv. Mater.* **2016**, *28 (43)*, 9581-9588, DOI: 10.1002/adma.201602173.

(62) Kazi, J.; Sen, R.; Ganguly, S.; Jha, T.; Ganguly, S.; Chatterjee Debnath, M., Folate Decorated Epigallocatechin-3-gallate (EGCG) Loaded PLGA Nanoparticles; in-Vitro and in-Vivo Targeting Rfficacy Against MDA-MB-231 Tumor Xenograft. *Int. J. Pharm.* **2020**, *585*, 119449, DOI: 10.1016/j.ijpharm.2020.119449.

(63) Oroojalian, F.; Beygi, M.; Baradaran, B.; Mokhtarzadeh, A.; Shahbazi, M. A., Immune Cell Membrane-Coated Biomimetic Nanoparticles for Targeted Cancer Therapy. *Small* **2021**, *17 (12)*, e2006484, DOI: 10.1002/smll.202006484.

(64) Miao, H.; Shen, R.; Zhang, W.; Lin, Z.; Wang, H.; Yang, L.; Liu, X. Y.; Lin, N., Near-Infrared Light Triggered Silk Fibroin Scaffold for Photothermal Therapy and

Tissue Repair of Bone Tumors. *Adv. Func. Mater.* **2020**, *31 (10)*, DOI: 10.1002/adfm.202007188.

(65) Keshtkar Vanashi, A.; Ghasemzadeh, H., Copper(II) Containing Chitosan Hydrogel as a Heterogeneous Fenton-like Catalyst for Production of Hydroxyl Radical: A Quantitative Study. *Int. J. Biol. Macromol.* **2022**, *199*, 348-357, DOI: 10.1016/j.ijbiomac.2021.12.150.

(66) Vines, D. C.; Green, D. E.; Kudo, G.; Keller, H., Evaluation of Mouse Tail-Vein Injections both Qualitatively and Quantitatively on Small-Animal PET Tail Scans. *J. Nucl. Med. Technol.* **2011**, *39 (4)*, 264-70, DOI: 10.2967/jnmt.111.090951.

(67) Liu, C.; Li, L.; Guo, Z.-P.; Lin, L.; Li, Y.-H.; Tian, H.-Y., PLG-g-mPEG Mediated Multifunctional Nanoparticles for Photoacoustic Imaging Guided Combined Chemo/Photothermal Antitumor Therapy. *Chinese J. Polym. Sci.* **2022**, *41 (4)*, 538-546, DOI: 10.1007/s10118-022-2857-3.

Table of Content (TOC)